Chapter 9

Appendix

9.1 Terminology of shear zones and shear zone networks

The **brittle-viscous** transition is the change from fracturing on one or more discrete surfaces to thermally activated creep within zones of viscous, solid-state flow (Schmid & Handy, 1991, Handy et al., in press). Following Ramsay & Huber (1983), we distinguish between **brittle shear zones** (synonymous with **faults** and **fractures**) and **ductile shear zones**. Shear zone without a prefix is a general term describing any zone with sub-parallel walls in which deformation is localized. We use the term ductile exclusively in relation to solid-state viscous, mylonitic deformation, being fully aware that ductility itself is not a mechanistic concept (Rutter, 1986, Schmid & Handy, 1991). The term **viscous** is used to describe deformation that was accommodated by thermally activated deformation mechanisms (Piorier, 1985). These include dislocation glide and dislocation creep, solid-state diffusion creep, diffusional mass transfer involving solution/precipitation and viscous grain boundary sliding (Schmid & Handy, 1991). Wherever special emphasize on deformation mechanisms is needed, we add appropriate prefixes.

Brittle shear zones show strain discontinuities across the shearing plane (marker 2 in Fig. 9.1a), whereas ductile shear zones show continuous variations of strain across their width and no geometrical discontinuities can be seen on the scale of the shear zone (marker 3 in Fig. 9.1a).

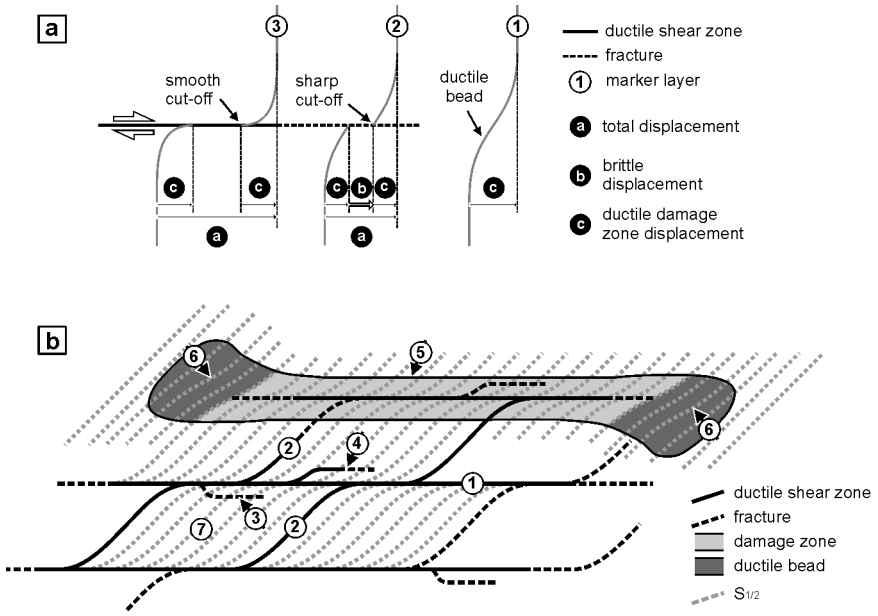

Figure 9.1: Features of shear zones and shear zone networks: (a) A mylonitic shear zone with a brittle tip. Deflected marker layers illustrate the monoclinal fold forming the ductile bead beyond the tip of the brittle fault (marker 1); a sharp cut-off towards the fault plane (marker 2) and a smooth cut-off towards the mylonitic shear zone centre (marker 3). Note the difference between the brittle displacement, the ductile damage zone displacement and the total displacement; (b) A shear zone network with host shear zones (1), step-over shear zones (2), a footwall drag truncation (3), a hanging wall drag truncation (4), the ductile damage zone (5) and a ductile bead (6) around a host shear zone.

Finite strain across ductile shear zones increases continuously from zero strain and displacement at the margins of the shear zone to maximum strain and displacement in its center. Brittle shear zones focus deformation on the shearing plane itself, but in most cases a volume of wall rock adjacent to the plane is deformed due to "the initiation, propagation, interaction and build-up of slip along faults" (Kim et al., 2004). In the fault mechanics literature, this volume is termed the "damage zone". Where markers are oriented at high angles to the fault as in this study, most of this deformation in the wall rock near the fault is expressed macroscopically as monoclinally folded markers, here termed **(ductile) fault drags**. The rock volume where such fault drags occur is termed the **ductile damage zone** (Fig. 3, 4, arrow 5 in Fig. 9.1b). The fault drag is **normal** when the deflection of markers is convex in the direction of shear along the fault or shear zone

(marker 3 in Fig. 9.1a), and is **reverse** when the deflection in the direction of shear is concave (Hamblin, 1965). The intersection between a dragged linear or planar marker and the fault plane is called a **cut-off** (Ramsay and Huber, 1983). The nature of cut-offs is important in the context of strain gradients and the transition from faults to ductile shear zones and we therefore distinguish between **smooth cut-offs** where the tangent to the deflected marker at the cut-off encloses an angle β with the shearing plane of $< 5°$ (Fig. 9.1a), and **sharp cut-offs** where $\beta > 5°$ (see markers in Fig. 3.4, Fig. 9.1a). Deflections of planar or linear markers next to a structural element cross-cutting the rock (e.g., a fault) have been named "flanking structures" (Passchier, 2001).

Monoclinal folds that form beyond the tips of brittle faults in the direction of tip propagation are termed **ductile beads**, following Elliott (1976). Elliott observed ductile beads in front of mode III fractures at the terminations of thrust faults. The ductile bead is part of the ductile damage zone (arrow 6 in Fig. 9.1b).

Displacement accommodated by ductile deformation in mylonitic shear zones is called **ductile displacement**. Displacement which is accommodated by ductile fault drags is called **ductile damage zone displacement** ('c' in Fig. 9.1a). Displacement accommodated by slip on brittle fault planes is termed **brittle displacement** ('b' in Fig. 9.1a). The sum of all displacements at a section across a shear zone - brittle and/or ductile - is the **total displacement,** D_{sect} ('a' in Fig. 9.1a). Distinguishing these different kinds of displacement is important when describing coeval discrete and distributed deformation.

The **width** of a shear zone along a particular section across the shear zone, W_{sect}, is measured perpendicular to the shearing plane. Shear strain distribution in shear zones reaches a maximum, γ_{max}, within the shear zone and can be averaged across the entire shear zone by dividing the total displacement by the width ($\gamma_{mean} = D_{sect}/W_{sect}$, see Appendix 9.2).

Shear zone networks consist of interconnected host- and step-over shear zones. **Host shear zones** are parallel to the bulk shearing plane ('1' in Fig. 9.1b). **Step-over shear zones** connect host shear zones at an angle to the overall shearing plane ('2' in Fig. 9.1b). Host and step-over shear zones isolate **lozenges** of less deformed host rock in between ('7' in Fig.

9.1b). Shear zones are found to widen by **drag truncation**, a process involving lateral branching of fractures along ductile shear zones into fault drags, combined with rotation and overprinting of the fabric in the sheared domains between the fault and the shear zone center. Drag truncation forms **truncated drag folds** or **truncated drags** ('3' and '4' in Fig. 9.1b).

9.2 Quantifying γ_{max} in shear zone centers

We measured the orientation of the existing S1/2 foliation along ten sections approximately perpendicular to the shear zone. The angle between the deflected S1/2 and the shear zone boundary (α') at a particular distance from the shear zone center was used to calculate shear strain (γ)/shear zone width (W_{sect})-diagrams (Fig. 3.5c) after Ramsay & Graham (1970):

$$\cot \alpha' = \cot \alpha - \gamma \tag{9.1}$$

where α is the angle between S1/2 and the shear zone boundary C3 before being sheared. This technique was developed for passive markers only, and using it for actively deforming markers - as shown for S1/2 by Carreras & García Celma (1982) - bears the risk of underestimating the finite shear strain. Nevertheless Eq. 9.1 gives a first-order estimate of γ.

Reliable γ values cannot be calculated near the shear zone center, because the angles between the deflected (and reactivated) S1/2 and C3 are very small, such that even small measurement errors render very large perturbations of γ. To calculate the maximum shear strain (γ_{max}) in these central parts of the shear zone, we constructed γ/W_{sect}-diagrams from the margins towards the shear zone center, as far as reliable measurements could be made (a and b in Fig. 9.2). We approximated functions $f(+x)$ and $f(-x)$ for the two scatter-plots resulting from measuring the deflection of S1/2 in the two fault drags. We then integrated these functions with respect to distance from the shear zone margins to the center:

$$A_x = \int_{-x}^{a} f(-x)dx \tag{9.2}$$

and

$$B_y = \int_{b}^{+x} f(+x)dx \tag{9.3}$$

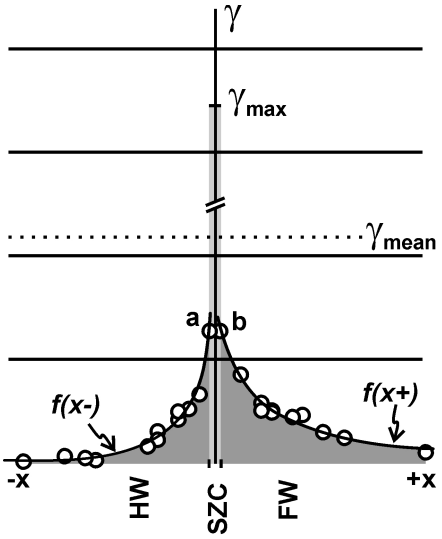

Figure 9.2: Shear strain vs. width (γ/W_{sect}) diagram. FW - footwall, HW - hanging wall, SZC - shear zone center. The shear strains were calculated using the equation of Ramsay & Graham (1970). The area of the grey rectangle in the shear zone center equals the part of the total displacement which was not accommodated by shearing in the drags. The rectangle represents a conservative approximation of the maximum shear strain in the shear zone center. See text for detailed explanation.

The area beneath the γ/W_{sect}-function equals the shear zone's total displacement at that particular site ($Dsect$, Ramsay & Graham, 1970), which can be estimated from independent measurements. Therefore,

$$C = D_{sect} - (A_x + B_y) \tag{9.4}$$

where C is the area of a rectangle whose base $\bar{ab}$ is the width of the shear zone centre, and whose length is a minimum estimate for γ_{max} (Fig. 9.2). The mean shear strain (γ_{mean}) accommodated by the shear zone along a given transect was calculated with the relation

$$\gamma_{mean} = D_{sect}/W_{sect} \tag{9.5}$$

9.3 Sample descriptions

- CC01 Metapsammite (44,6% quartz, 24,1% biotite, 15,4% plagioclase, 9,8% muscovite, 4,0% opaque undefined ore phase, accessory epidote, tourmaline). Cala Prona. Collected from the center of the mylonitic shear zone in Fig. 4.2, about 16m NW of the shear zone termination (cf. Fig. 3.5).

- CC05 Metapsammite (48,8% quartz, 30,6% biotite, 7,6% plagioclase, 5,4% muscovite, 4,8% k-feldspar, accessory epidote, tourmaline). Cala Prona, see Fig. 4.2 for location.

- CC08 Metapelite (46,8% biotite, 25,6% quartz, 16,1% feldspar, 4,2% chlorite, accessory muscovite, ilmenite and tourmaline). Cala Prona, see Fig. 4.2 for location.

- CC11a-c pure vein Qtz, sampled along dragged quartz vein. Cala Serena, UTM 31T 521835 east, 4687155 north.

- CC12a Metapelite (45,6% quartz, 34,8% biotite, 11,2% feldspar, accessory garnet, chlorite, muscovite, ilmenite and tourmaline). Cala Serena, UTM 31T 521822 east, 4687045 north.

- CC14b Metapsammite (44,4% quartz, 25,5% biotite, 20,5% feldspar, 3,5% muscovite, accessory ilmenite, chlorite and tourmaline). Cala Serena, see Fig. 7.1 for sample location, UTM 31T 521859 east, 4687052 north.

- CC17a Metapsammite (44,5% quartz, 24,4% feldspar, 23% biotite, 6% muscovite, accessory garnet, ilmenite, chlorite, apatite and tourmaline). Cala Serena, see Fig. 9.4 for location.

- CC17c Metapsammite (41,2% quartz, 28,2% feldspar, 24,8% biotite, 4,6% chlorite, accessory garnet, ilmenite, apatite and tourmaline). Cala Serena, see Fig. 9.4 for location.

- CC18 Metapelite (39,4% quartz, 32% biotite, 24,2% feldspar, 4,4% muscovite, accessory garnet, ilmenite, chlorite, apatite and tourmaline). Cala Serena, see Fig. 9.4 for location.

- CC31 Metapsammite (41,5% quartz, 26,9% feldspar, 26,5% biotite, 3% muscovite, accessory ilmenite, chlorite, apatite and tourmaline). Cala Serena, see Fig. 9.4 for location.
- CC37/1 Metapsammite (49,4% quartz, 30,9% biotite, 14% feldspar, 1,6% muscovite, accessory ilmenite, chlorite and tourmaline). Cala Prona, see Fig. 4.2 for location.
- CC37/2 Metapelite (41,4 % biotite, 36,3% quartz, 15,1% feldspar, 2,8% muscovite, accessory ilmenite, chlorite and tourmaline). Cala Prona, see Fig. 4.2 for location.
- CC38 Metapsammite (47,7% quartz, 35% biotite, 14,3% feldspar, 0,9% muscovite, accessory ilmenite, chlorite and tourmaline). Cala Prona, see Fig. 4.2 for location.
- CC52 Metapelite (35,0% quartz, 33,1% biotite, 26,3% feldspar, 6,6% muscovite). Cala Serena, see Fig. 9.4 for location.
- CC105 Metapsammite (45,4% quartz, 33,3% biotite, 15,3% feldspar, 3,9% muscovite, accessory ilmenite, chlorite and tourmaline). Cala Serena (see Fig. 9.4 for location.

Quartz samples that were used to determine differential stresses are 100% pure quartz. Their locations are marked in Fig. 9.4, with the exception of sample CC11, which is given above.

9.4 Element distribution maps to Fig. 4.11

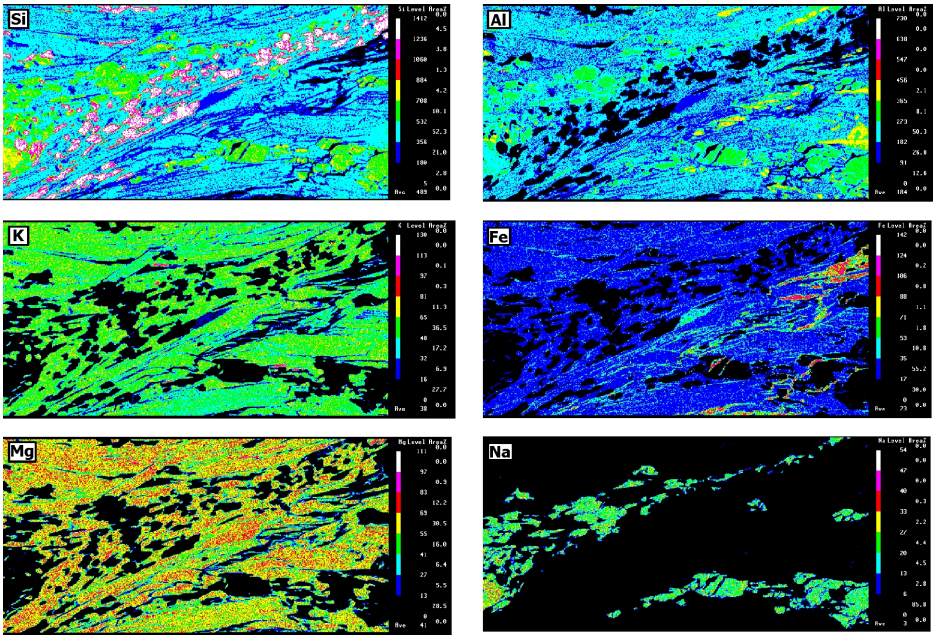

Figure 9.3: Element distribution map from shear band in Fig. 4.11. Fault rock in shear band is composed of Qtz2, Plag2, Bt2 and Ilm. See Fig. 4.11 for scale and text for explanation. Sample CC37/2.

9.5 Figure- and sample locations

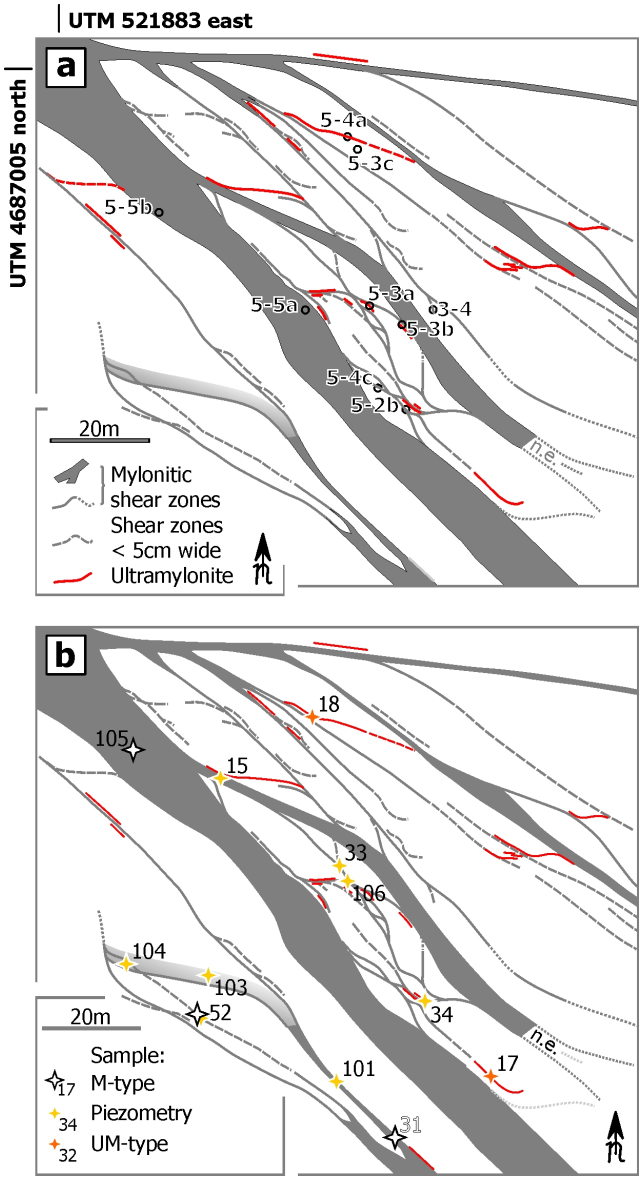

Figure 9.4: (a) Locations of outcrops shown on figures in the text. Labeling corresponds to the figure numbers in the text. (b) Sampling sites of samples investigated in this paper and shown on figures in the text. Labeling corresponds to the sample numbers in the text, without the 'CC'-prefix.

9.6 Measurement of shear zones

Shear zone length is the length of the polyline defining the shear zone center (Fig. 9.5). Shear zone width W_{sect} is measured normal to the shear zone center at the location of maximum displacement. These criteria could not be used for the largest-scale data due to the lack of appropriate markers. In order to define their lengths and widths shear zones were vectorized as polygons from Fusseis et al. (2006). Feret´s diameter (i.e. the longest distance between any two points along the shear zone boundary) was determined with the image analysis software ImageJ and taken as shear zone length (Fig. 9.5). Hence, the length of branching and/or curved shear zones is underestimated for the large-scale data. The width was measured at the widest position along the shear zone, normal to the main strike direction at that point (Fig. 9.5).

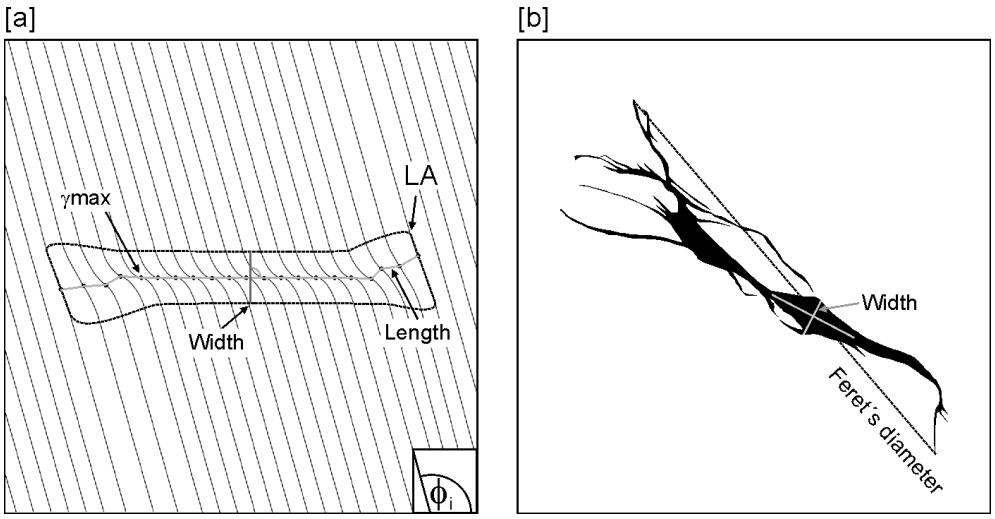

Figure 9.5: Measurement of shear zones. See text for explanation.

9.7 Determination of the representative area (RA)

Consider a foliation map with foliation traces at angles ϕloc and ϕi to a reference line, respectively, inside and outside a shear zone (Fig. 9.6). In n runs, this foliation map is covered with grids (area of interest, $AOIa_n$)

comprising square cells, x_{ai}, whose base length increases following $a_n = a_0 \cdot 2^{n-1}$, where a_0 is the initial, shortest base length (Fig. 9.6. Within any one of the square cells of the $AOIa_n$, the mean orientation of all foliation traces, ϕmi, is calculated with ACFs (see below). A cell is classified to be outside of the shear zone if $\phi mi \in \phi i$ (unlocalized orientations) and within the shear zone if $\phi mi \notin \phi i$ (localized orientations). The frequency distribution of elements with mean orientations that are localized, Freq(ϕloc), is calculated for each run (i.e. for a given a_n) and plotted against the width of the grid cells (Fig. 9.6b). The value of a_n at which Freq(ϕloc) = 5% is arbitrarily designated as the width a_{RA} and corresponds to one side of the square representative elementary area, RA:

$$RA = a_{RA}^2 \tag{9.6}$$

The value of a_{RA} is easily determined by interpolating linearly between points bracketing the 5%-boundary on a plot of Freq(ϕloc) versus the base lengths of the grid cells (Fig. 9.6c). Note that this method had to be simplified for the largest-scale data due to the lack of fabric within the shear zones and a $\phi i = [10°; 110°]$. The shear zone areas were vectorized and filled with a homogeneous, linear pattern parallel to their main strike direction, assuming that the fabric in the shear zone center is approximately parallel to average shear zone trend. The remaining map was filled with another homogeneous, linear pattern at a high angle to represent undeflected passive markers.

9.8 Determining ϕmi with Autocorrrelation Functions

This section describes how to determine the mean foliation orientation, ϕmi within a grid cell x_{ai} of an area of interest. The Autocorrrelation Function (ACF) is a statistical function that describes the spatial variability of regionalized variables. The ACF may be written:

$$f(x,y) \otimes f(x,y) = \int_{-\infty}^{\infty} \int_{-\infty}^{\infty} f(x',y') \cdot f(x+x', y+y') dx' dy' \tag{9.7}$$

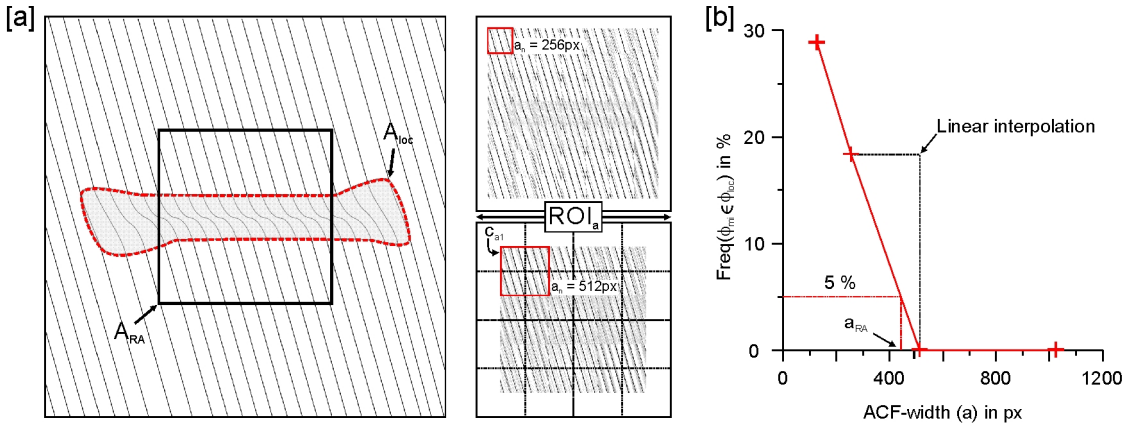

Figure 9.6: Determination of RA from foliation trajectory maps and equivalent image data. (a) Image of a shear zone of area LA indicated by the shaded polygon. The foliation map is covered with grids comprising squares whose base length a_n increases in several runs. For a given a_n, ACFs (c_{ai}) are calculated for each grid cell. (b) Freq(ϕloc) against ACF-size in pixels. See Text for explanation.

where $f(x, y)$ represents the two-dimensional brightness function defining the sample image, the operator $\otimes$ stands for a correlation or convolution, and x' as well as y' are the dummy variables of integration (Panozzo Heilbronner 1992). The value of the ACF at a given point (x,y), ρ, yields the correlation of all image points $(x + x', y + y')$ with all neighborhood points (Panozzo Heilbronner 1992). The origin of the ACF coordinate system is located at the center of the ACF figure (Figs. 9.7a,b). The ACF figure allows one to see how well an image correlates with itself when it is replaced with respect to itself in all possible directions (Panozzo Heilbronner 1992). Thus, it reveals low gradients in ρ parallel to elongate feature directions or to features with low spatial frequencies[1], and high gradients in ρ parallel to short feature directions or to features with high spatial frequencies (fig. 4 in Panozzo Heilbronner 1992). This property is what allows ACF figures to be used to determine directions of preferred orientation, for example, the shape-preferred orientation of platy or elongate minerals in rocks (Panozzo Heilbronner 1992, Heilbronner 2002).

In this paper, we apply ACFs to determine the mean orientation of foliation trajectories from 2D images like maps and thin sections. For a given AOIa, center-weighted ACFs are calculated for each x_{ai} to obtain the mean orientation of the foliation within that cell. The x_{ai} overlap 1/2 of their size in both horizontal and vertical directions ensuring the ACF-center c_{ai} being measured four times smoothing local variations of the ACF.

A cell typically contains several foliation traces, one or more of which may have different orientations. All of these traces determine the geometry of the ACF figure to an extent dependent on their shape, orientation and frequency. Thus, the ACF averages the orientations of all objects (foliations) within a given cell. We used center-weighted ACFs to smooth out local aberrations in the orientation of foliation traces (Fig. 9.7b). The long axis of the central ACF peak in the x´-y´-plane yields the mean orientation ϕmi of the foliation in an analyzed grid cell of the AOIa (Fig. 5c in Panozzo Heilbronner 1992).

[1]This is the frequency at which an object reoccurs within the image, e.g. the spacing of foliation traces.

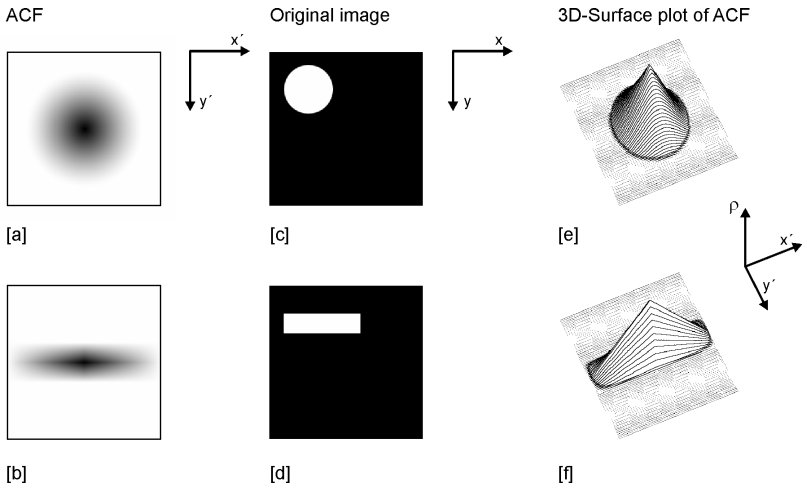

Figure 9.7: Visualization of the ACF. [a] and [b] show ACFs for sample images in [c] and [d]. [e] and [f] show two 3D-surface plot of the ACFs. Zero displacement is always located in the ACF center. Therefore, the highest ACF-peaks (right column) indicate maximum correlation in the ACF centers. The gradient of the ACF-brightness depends on the shape of the analyzed object.

9.9 Thresholding of ACF data

We used macros for de-noising the ACF data, which can, together with a detailed manual, be obtained from Christoph Schrank. Thresholding is the process of 'cutting off' the central ACF peak from the background noise. The shape and orientation of the central ACF peak depend on the gray value chosen to define its basal contour (Fig. 9.7a, b). This peak rises above a plane that consists of valleys and ridges (Fig. 9.8c). For image displacements smaller than the average marker line distance, small correlations are responsible for the valleys due to small overlaps of oblique or curved markers. This is unavoidable background correlation (Panozzo Heilbronner, 1992). If the displacement comes close to the average marker line distance, the overlaps increase on account of the periodicity of the foliation pattern causing ridges of higher correlation. Since the basal contour of the central peak is of interest only, it must be 'cut off' not only above the background correlation level, but also such that no contacts to the adjacent ridges occur. This is necessary because the 'cut-off' is done by binary thresholding of the gray values in the regarded image: all values equal to or above the threshold are converted to black whereas those below the threshold become

white. If the threshold is too low, the central peak as well the major ridges are connected. As a consequence, this c_{ai} contains a large, quasi rectangular particle that does not yield the orientation of the central peak when determined automatically by a bitmap analysis software. Since the gray value distribution of the c_{ai} is positively skewed (Fig. 9.8d), we propose to calculate the threshold simply by adding the mean gray value and its standard deviation. This proved to yield good results (Fig. 9.8e).

After thresholding, all remnant ridge-related particles as well as single-pixel noise are removed by a routine simply selecting the central particles and pasting them in a blank image (Fig. 9.8f). Otherwise, the automatic image analysis routine measuring the orientations of the central particles would regard the noise as well and bias the results. The ACF-data in the present paper have been calculated, processed and evaluated using the public domain software Scion Image (http://www.scioncorp.com/) and macros by Heilbronner (2002).

9.10 Testing the robustness of the ACF method

Because the ACF figure depends on the geometry, frequency, and distribution of the marker lines in the sample image, bias must be expected according to variations of these features. Assuming careful mapping, the geometrical bias is caused by variations of marker line thickness. Thick marker lines reduce the average marker line distance. This results in a higher background correlation level because the overlaps due to the periodic foliation pattern occur for smaller displacements (Fig. 9.9a). The height of the central peak compared to the basal plane decreases. Thus, thresholding and de-noising are rendered more difficult because the skewness of the gray value distribution is diminished. The probability of connected particles is augmented. The proportion of x_{ai} with $\phi mi \in \phi i$ increases as well (Fig. 9.9d). This effect becomes more relevant for ACF-sizes close to the average marker line distance. Thus, huge line thickness should be avoided. Based on empirical considerations, we used a line thickness of one point, the horizontal image width being 1024 pixel.

The frequency and distribution of marker lines depend on rock properties and outcrop conditions. Gaps in maps due to lack of outcrop are common.

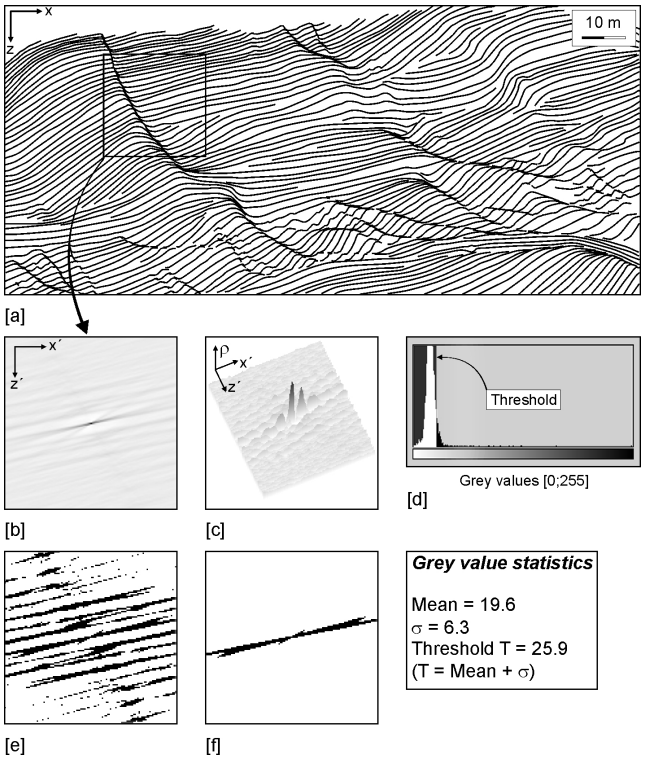

Figure 9.8: Thresholding and de-noising of ACF-centers, c_{ai}. [a] Foliation map of the Cala Cullaró area (Fig. 1c). Box with arrow marks a sample x_{ai}. [b] c_{ai} corresponding to x_{ai} indicated in [a] in plane view. The origin of the coordinate system is in the image center. Gray values relate to the correlation level ρ yielded by the ACF for a given displacement with black (=255) being equivalent to ρ and white (=0) notifying zero correlation. [c] 3D-plot of the same c_{ai}. [d] Histogram of c_{ai}. [e] c_{ai} after application of the proposed threshold. Note the central particle being separated from the remnant ridge particles. [f] c_{ai} after thresholding and de-noising. Only the basal contour of the ACF-peak is left.

For heterogeneous foliation maps with major gaps in line distribution, the background correlation level of the ACF decreases (Fig. 9.9b). Most segments of the marker lines usually have a non-localized orientation, ϕi. So the gaps in line density locally cause a reduction of periodic overlaps for displacements close to the average marker line distance. The frequency of x_{ai} with $\phi mi \in \phi i$ is artificially reduced at these places. This effect increases for decreasing ACF-size because the gaps become large compared to ACF-size. The graph in the Freq($\phi mi \in \phi i$) versus ACF-size plot is shifted upwards (Fig. 9.9d). The differences in the graphs decrease significantly at the scale of aRA (Fig. 9.9d).

We conclude: the divergence in the graphs depends on variations in the average marker line distance and gaps in the marker line distribution. If the scale of these spatial features is small compared to the ACF size, this bias is averaged out. This is the case at the scale of aRA because the average marker line distance is determined by the size of the smallest anisotropies regarded which are intrinsically small compared to RA due to the geometric homogeneity condition. Nevertheless, where reasonably applicable we used linear interpolations to carefully fill gaps between the marker lines (Fig. 9.9c).

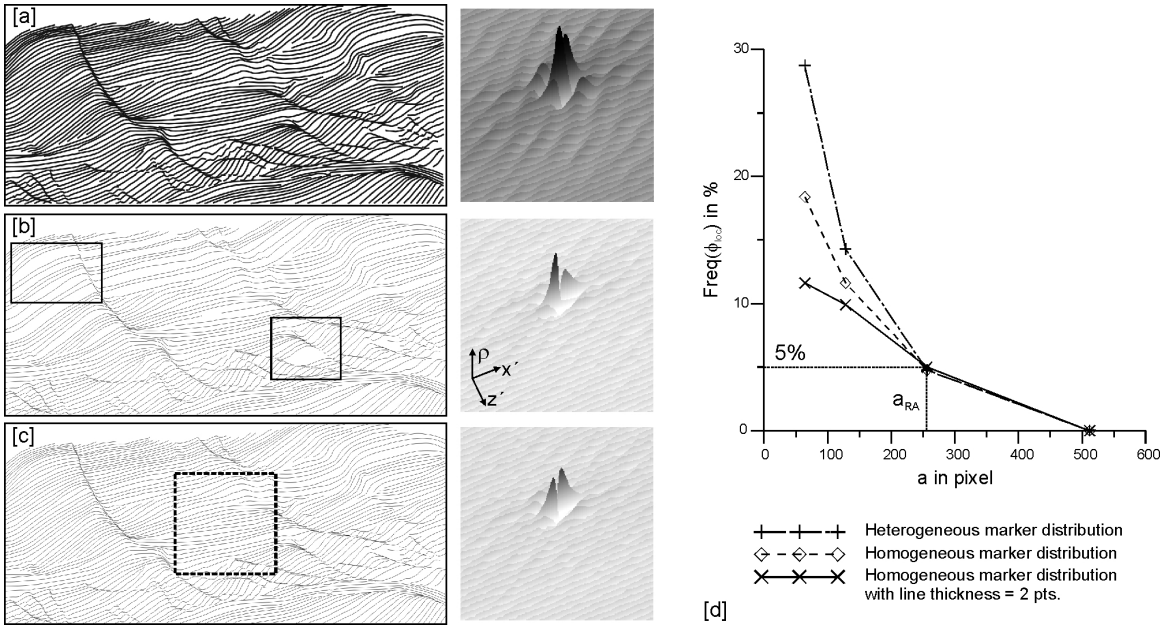

Figure 9.9: Influence of marker line distribution and line thickness on RA. [a] - [c] Three versions of a foliation map including close-up view of the related ACF-peak calculated for the central image area (dashed square in [c] shows location of x_{ai}). Note that the vertical axes are scaled in a way that peak maximum is always at the same height. See text for explanation. [a] Homogenized foliation map with line thickness = 2 points. [b] Heterogeneous foliation map of line thickness = 1 point exposing major gaps in line distribution (examples marked by rectangles). [c] Homogenized foliation map of line thickness = 1 point. [d] Plot of Freq(*philoc*) versus ACF-size for all sample images.

9.11 Thermometric data from samples CC17a and CC17c

ID	Ti	X(Mg)	T(C)	
BT17a_040106-12	0,0955	0,5074	370,45	Matrix
BT17a_040106-13	0,0935	0,5076	359,37	Matrix
BT17a_040106-14	0,0987	0,5225	396,63	Matrix
BT17a_040106-15	0,0977	0,5435	406,10	Matrix
Line 3 Grt17a 040106_Bt-Grt	0,0979	0,5116	385,75	Matrix
Line 5 Grt17a 040106_Bt-Grt	0,0954	0,5361	390,08	Matrix
Line 10 Grt17a 040106_Bt-Grt	0,1036	0,5408	428,48	Matrix
Line 11 Grt17a 040106_Bt-Grt	0,1075	0,5349	439,05	Matrix
Line 12 Grt17a 040106_Bt-Grt	0,1032	0,5292	420,19	Matrix
biot17c_161205_2	0,1176	0,5482	476,66	Matrix
Grid 2-3 grid on 17c_54	0,0903	0,4431	282,36	Matrix
Grid 6-1 grid on 17c_54	0,0861	0,5122	310,31	Matrix
biot17c_161205_7	0,1078	0,5456	446,07	Matrix
biot17c_161205_9	0,0892	0,5400	358,90	Matrix
Biot17	0,0897	0,5138	339,94	Matrix
Biot18	0,1000	0,5181	399,84	Matrix
Biot19	0,0962	0,5179	381,38	Matrix
Biot20	0,1722	0,5040	561,23	Matrix
Biot1	0,1104	0,5503	456,94	Clast
Biot2	0,1068	0,5348	436,77	Clast
Biot3	0,1140	0,5411	463,25	Clast
Biot4	0,1132	0,5367	458,33	Clast
Biot5	0,1129	0,5430	460,91	Clast
Biot6	0,1222	0,5386	484,10	Clast
Biot7	0,1393	0,5230	515,21	Clast
Biot8	0,1035	0,4945	401,33	Clast
Biot9	0,1218	0,5513	489,04	Clast
Biot10	0,1089	0,5476	450,80	Clast
Biot11	0,1072	0,5670	456,34	Clast
Biot12	0,1138	0,5358	459,98	Clast
Biot13	0,1050	0,5417	434,08	Clast
Biot14	0,1067	0,5335	435,60	Clast
Biot15	0,1151	0,5102	451,29	Clast
Biot16	0,0958	0,5245	383,95	Clast
Biot34	0,1061	0,5064	418,37	Clast
Biot35	0,0968	0,5124	380,91	Clast
Biot36	0,1056	0,5333	431,63	Clast
Biot38	0,0828	0,4798	232,68	Clast
Biot39	0,1186	0,4858	450,58	Clast
Biot40	0,1192	0,4933	455,62	Clast
Biot43	0,1234	0,5099	474,49	Clast
Biot44	0,1148	0,5051	448,00	Clast
Biot45	0,1156	0,5110	453,01	Clast
Biot46	0,1092	0,4983	425,77	Clast
Biot47	0,1067	0,4457	389,50	Clast

Table 9.1: Ti in Bt-data as illustrated in Fig. 5.12 (1/3). Samples CC17a and CC17c. See text for explanation, Table 5.2 for representative compositions and Fig. 9.4 for sample location.

ID	Ti	X(Mg)	T(C)	
Line 1 Biot_clast2_line1	0,1096	0,5117	433,87	Clast2 line
Line 2 Biot_clast2_line1	0,1041	0,5102	412,52	Clast2 line
Line 4 Biot_clast2_line1	0,1159	0,5344	465,33	Clast2 line
Line 5 Biot_clast2_line1	0,1243	0,4613	457,05	Clast2 line
Line 6 Biot_clast2_line1	0,1180	0,5455	476,47	Clast2 line
Line 7 Biot_clast2_line1	0,1232	0,4837	463,03	Clast2 line
Line 8 Biot_clast2_line1	0,1191	0,4375	432,59	Clast2 line
Line 9 Biot_clast2_line1	0,0884	0,4877	306,61	Clast2 line
Line 10 Biot_clast2_line1	0,1184	0,5170	464,20	Clast2 line
Line 11 Biot_clast2_line1	0,1134	0,5114	446,50	Clast2 line
Line 12 Biot_clast2_line1	0,1193	0,4466	436,86	Clast2 line
Line 13 Biot_clast2_line1	0,1237	0,5094	474,95	Clast2 line
Line 14 Biot_clast2_line1	0,1168	0,4677	437,55	Clast2 line
Line 15 Biot_clast2_line1	0,1129	0,4313	408,30	Clast2 line
Line 16 Biot_clast2_line1	0,1037	0,5131	412,83	Clast2 line
Line 17 Biot_clast2_line1	0,1054	0,4947	409,16	Clast2 line
Line 18 Biot_clast2_line1	0,1056	0,5057	415,99	Clast2 line
Line 19 Biot_clast2_line1	0,1060	0,5014	415,25	Clast2 line
Line 20 Biot_clast2_line1	0,1111	0,5154	440,94	Clast2 line
Line 21 Biot_clast2_line1	0,1079	0,4998	421,74	Clast2 line
Line 22 Biot_clast2_line1	0,1077	0,4415	392,09	Clast2 line
Line 23 Biot_clast2_line1	0,1058	0,4918	409,45	Clast2 line
Line 24 Biot_clast2_line1	0,1112	0,4933	430,24	Clast2 line
Line 25 Biot_clast2_line1	0,1027	0,4455	370,46	Clast2 line
Line 26 Biot_clast2_line1	0,0870	0,5153	321,54	Clast2 line
Line 27 Biot_clast2_line1	0,1035	0,4630	383,69	Clast2 line
Line 28 Biot_clast2_line1	0,1732	0,4616	550,62	Clast2 line
Line 1	0,1117	0,4453	409,91	Clast2 line
Line 2	0,1131	0,4405	413,08	Clast2 line
Line 3	0,1140	0,5033	444,42	Clast2 line
Line 4	0,1185	0,4331	428,82	Clast2 line
Line 5	0,1098	0,4953	426,29	Clast2 line
Line 6	0,1164	0,5413	469,98	Clast2 line
Line 7	0,1216	0,5004	465,57	Clast2 line
Line 8	0,1123	0,5061	440,17	Clast2 line
Line 9	0,1172	0,5259	464,79	Clast2 line
Line 10	0,1239	0,4632	456,87	Clast2 line
Line 11	0,1248	0,4884	469,05	Clast2 line
Line 12	0,1190	0,4745	447,15	Clast2 line
Line 13	0,1269	0,4689	467,04	Clast2 line
Line 14	0,1248	0,4887	469,23	Clast2 line
Line 15	0,1080	0,4905	417,30	Clast2 line
Line 16	0,1181	0,4949	453,15	Clast2 line
Line 17	0,1154	0,4707	434,03	Clast2 line
Line 18	0,1230	0,5040	470,76	Clast2 line
Line 19	0,1131	0,4903	435,33	Clast2 line
Line 20	0,1183	0,4818	448,04	Clast2 line

Table 9.2: Ti in Bt-data as illustrated in Fig. 5.12 (2/3). Samples CC17a and CC17c. See text for explanation, Table 5.2 for representative compositions and Fig. 9.4 for sample location.

ID	Ti	X(Mg)	T(C)	
Line 21	0,1119	0,4702	421,69	Clast2 line
Line 22	0,1188	0,4525	437,37	Clast2 line
Line 23	0,1197	0,4288	431,14	Clast2 line
Line 24	0,1074	0,5188	430,03	Clast2 line
Line 25	0,1170	0,5243	463,61	Clast2 line
Line 26	0,1192	0,4755	447,98	Clast2 line
Line 27	0,1079	0,4901	416,65	Clast2 line
Line 28	0,1182	0,4344	428,37	Clast2 line
Line 29	0,1147	0,5055	447,75	Clast2 line
Line 30	0,1144	0,4857	437,71	Clast2 line
Line 31	0,1187	0,4585	439,45	Clast2 line
Line 32	0,1139	0,5058	445,29	Clast2 line
Line 33	0,1139	0,5115	448,14	Clast2 line
Line 34	0,1189	0,5009	458,15	Clast2 line
Line 35	0,1147	0,4960	443,40	Clast2 line
Line 36	0,1174	0,4722	441,03	Clast2 line
Line 37	0,1207	0,5286	475,73	Clast2 line
Line 38	0,1147	0,5269	458,19	Clast2 line
Line 39	0,1211	0,4870	458,41	Clast2 line
Line 40	0,1174	0,5124	459,13	Clast2 line
Line 41	0,1167	0,5111	456,39	Clast2 line
Line 42	0,1254	0,5499	497,01	Clast2 line
Line 43	0,1094	0,4816	418,02	Clast2 line
Line 44	0,1185	0,5071	459,85	Clast2 line
Line 45	0,1203	0,4937	459,16	Clast2 line
Line 46	0,1187	0,4687	443,74	Clast2 line
Line 47	0,1203	0,5102	466,25	Clast2 line
Line 48	0,1154	0,4745	435,64	Clast2 line
Line 49	0,1151	0,4925	442,81	Clast2 line
Line 50	0,1102	0,4411	402,12	Clast2 line
Line 51	0,1124	0,4729	424,79	Clast2 line
Line 52	0,0990	0,5060	387,43	Clast2 line
Line 53	0,0990	0,5166	394,17	Clast2 line
Line 54	0,1058	0,4824	404,36	Clast2 line
Line 55	0,0971	0,4801	361,13	Clast2 line
Line 56	0,1099	0,5088	433,72	Clast2 line
Line 57	0,0980	0,4223	329,84	Clast2 line
Line 58	0,1050	0,4812	400,50	Clast2 line
Line 11	0,1248	0,4884	469,05	Clast2 line
Line 12	0,1190	0,4745	447,15	Clast2 line
Line 13	0,1269	0,4689	467,04	Clast2 line
Line 14	0,1248	0,4887	469,23	Clast2 line
Line 15	0,1080	0,4905	417,30	Clast2 line
Line 16	0,1181	0,4949	453,15	Clast2 line
Line 17	0,1154	0,4707	434,03	Clast2 line
Line 18	0,1230	0,5040	470,76	Clast2 line
Line 19	0,1131	0,4903	435,33	Clast2 line
Line 20	0,1183	0,4818	448,04	Clast2 line

Table 9.3: Ti in Bt-data as illustrated in Fig. 5.12 (3/3). Samples CC17a and CC17c. See text for explanation, Table 5.2 for representative compositions and Fig. 9.4 for sample location.